

Faint Radio Sources and Star Formation History

D. B. Haarsma

Calvin College, 3201 Burton Street SE, Grand Rapids, MI 49546 dhaarsma@calvin.edu

R. B. Partridge

Haverford College, Haverford, PA 19041 bpartrid@haverford.edu

R. A. Windhorst and E. A. Richards¹

Department of Physics & Astronomy, Arizona State University, Tempe, AZ, 85287-1504
rogier.windhorst@asu.edu, eric.richards@asu.edu

ABSTRACT

The centimeter-wave luminosity of local radio galaxies correlates well with their star formation rate. We extend this correlation to surveys of high-redshift radio sources to estimate the global star formation history. The star formation rate found from radio observations needs no correction for dust obscuration, unlike the values calculated from optical and ultraviolet data. Three deep radio surveys have provided catalogs of sources with nearly complete optical identifications and nearly 60% complete spectroscopic redshifts: the Hubble Deep Field and Flanking Fields at 12h+62d, the SSA13 field at 13h+42d, and the V15 field at 14h+52d. We use the redshift distribution of these radio sources to constrain the evolution of their luminosity function. The epoch dependent luminosity function is then used to estimate the evolving global star formation density. At redshifts less than one, our calculated star formation rates are significantly larger than even the dust-corrected optically-selected star formation rates; however, we confirm the rapid rise from $z = 0$ to $z = 1$ seen in those surveys.

Subject headings: cosmology: observations — radio continuum:galaxies — galaxies: evolution — galaxies: luminosity function — stars: formation — galaxies: starburst

1. Introduction

In the last few years, a variety of observational methods have been used to study the global star formation history of the universe at a range of redshifts. Figure 1 compiles the results from several of these studies, scaling all to the same cosmology and IMF. In plotting the points, we

¹Hubble Fellow

used the corrections for extinction by dust calculated by Steidel et al. (1999, their figure 9). The diagram shows significant scatter in the star formation density at each redshift. Most studies agree, however, that the star formation density rises rapidly from $z = 0$ to $z = 1$. Beyond a redshift of 1 it is unclear whether the star formation density decreases significantly (as suggested at first by Madau et al. 1996) or stays roughly constant (for example, Steidel et al. 1999).

Radio observations have important advantages in determining the global star formation history, and are a useful complement to studies at other wavelengths. Unlike calculations based on ultraviolet and optical observations, there is no need to make uncertain corrections for dust extinction since the radio emission at $\nu \gtrsim 1$ GHz passes freely through dust. Compared to far-infrared and submillimeter studies, interferometric radio observations typically have better positional accuracy, allowing for more reliable identifications with objects detected at other wavelengths (Richards 1999; Downes et al. 1999). Finally, since far-infrared emission is due to re-heated dust, the original source of energy (whether star formation or AGN) can be unclear; radio properties, such as spectral index and morphology, can help distinguish between these. We do note, however, that contamination of the radio flux by emission from AGN is a problem (addressed in §2.5). In addition, relatively few high redshift star-forming radio sources have as yet been detected (though current and planned deep radio surveys will rapidly change that). As a consequence, the statistical sample used in this work is small.

Our strategy in this paper is as follows. We use very sensitive radio surveys to detect star forming galaxies at high redshift. Not all of the sources in these surveys are star-forming (some are probably AGN), but we deal with this problem by defining data samples that give lower and upper limits to the star formation history, as described in §2. Next, in §3, we use these data to determine the evolving luminosity function for star-forming radio sources. The redshift and flux distribution of the sources, as well as the total extragalactic radio background, are used to constrain the evolution. In §4, we use the well-known relationship between radio luminosity and star formation rate (and discuss the assumption that this relationship holds for all redshifts) to find the star formation history directly from the observed radio sources. The evolving luminosity function is used to correct for faint sources below the observational detection limits. We discuss our conclusions in §5.

Unless stated otherwise, we assume a cosmology of $H_0 = 50$, $\Omega_m = 1$, and $\Omega_\Lambda = 0$, and a non-evolving Salpeter Initial Mass Function with a stellar mass range of $0.1 - 100M_\odot$. We use a radio spectral index of $\alpha = 0.4$ (where $S \propto \nu^{-\alpha}$), which is appropriate for faint sources selected at 5 or 8 GHz (Windhorst et al. 1993; Richards 2000).

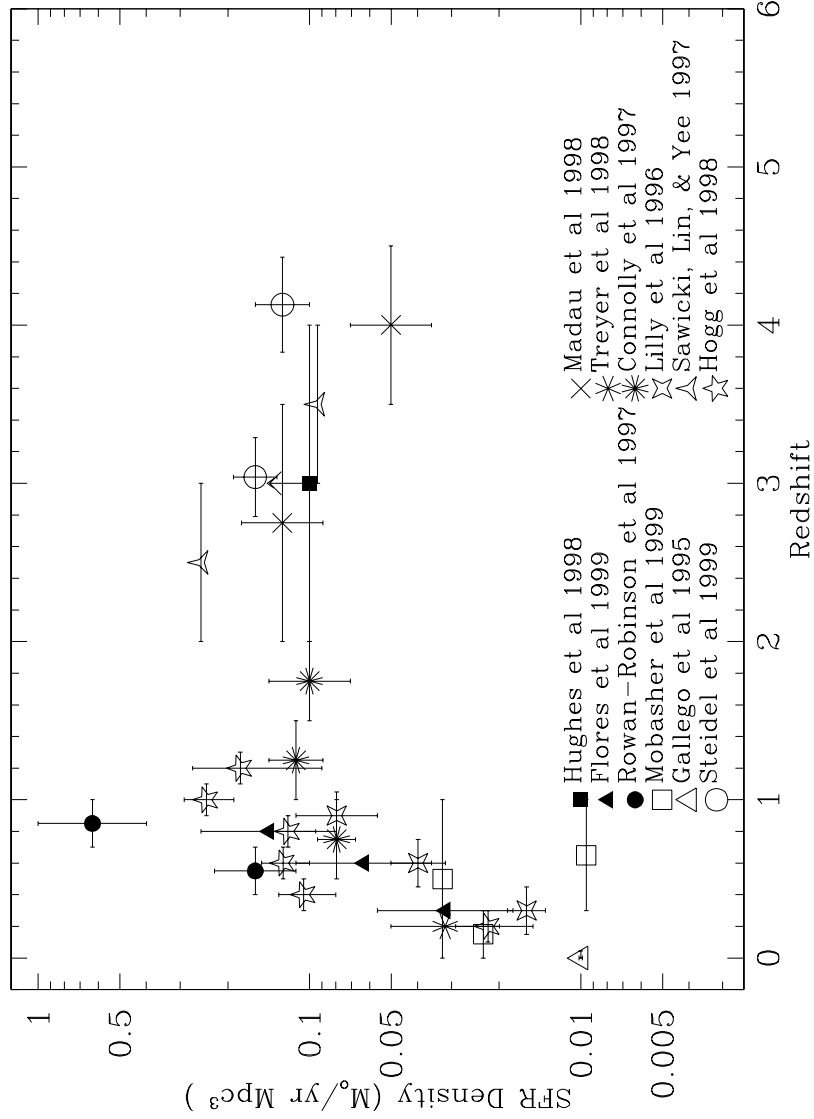


Fig. 1.— Some star formation histories at various wavelengths. All the data points are scaled to $H_0 = 50, \Omega_m = 1, \Omega_\Lambda = 0$, and a Salpeter Initial Mass Function from $0.1-100M_{\odot}$ (following the scaling by Baugh et al. 1998, their figure 16). Corrections for dust extinction calculated by Steidel et al. (1999, their figure 9) were used.

2. The Data Sets

2.1. Surveys

Three fields have been observed to micro-Jansky sensitivities at centimeter wavelengths and also have extensive photometric and spectroscopic data: the Hubble Deep Field (HDF) at 8 GHz (Table 2), the SSA13 field at 8 GHz (Table 3), and the V15 field at 5 GHz (Table 2). Table 1 summarizes information on the three fields, all of which were observed at the Very Large Array (VLA²). Tables 2, 3, and 4 list the individual sources in each field; the columns are as follows:

Column 1: The source name.

Columns 2,3: S_8 , S_5 , and $S_{1.4}$ are the radio flux densities at 8 GHz, 5 GHz, and 1.4 GHz respectively. If a measured value of $S_{1.4}$ is not available, we use the spectral index shown in Column 4 to calculate $S_{1.4}$ and list the value in parentheses in Column 3.

Column 4: The radio spectral index, α , defined as $S \propto \nu^{-\alpha}$. If 1.4 GHz measurements are not available, we use assume a spectral index of 0.4 unless this violates the survey detection threshold at 1.4 GHz.

Column 5: The primary beam correction factor, B_i (see §2.2, eq. 1).

Column 6: The galaxy type (see §2.4): *sim* refers to spiral, irregular, or merger; *el* refers to elliptical; *fr* refers to faint ($I > 25$) or red ($I - K > 4$); and *un* refers to unknown type or undetected. The galaxy type in parentheses is the assumed galaxy type in the case of *un*.

Column 7: The redshift type (see §2.3): *sp* refers to spectroscopic, *ph* refers to rough photometric (based on I or HK' magnitudes), *a* refers to random assignment, and *afr* refers to random assignments for galaxies of type faint/red.

Column 8: The redshift used in calculations.

Columns 9,10: The I and HK' magnitudes. K magnitudes are converted to HK' magnitudes by $K = HK' - 0.3$.

Column 11: The maximum redshift, z_{max} , at which the galaxy would have been detected, based on its emitted luminosity $L_{e,1.4}$.

Column 12: The log of the luminosity emitted at 1.4 GHz.

Column 13: The star formation rate for each individual galaxy, derived from its radio luminosity ($L_{e,1.4}$) and equation 15. If the source is elliptical (or assumed elliptical), the emission is probably contaminated by AGN and the calculated star formation rate is only an upper limit. For some of these sources, the AGN contamination causes the calculated star formation rate to be unphysically large (greater than $5000M_{\odot}/yr$), so it does not provide an interesting upper limit and we do not list it; we do, however, include these sources in our “upper” sample to give conservative upper limits on our results.

Column 14: The samples to which the source was assigned (see §2.5): *U* refers to the upper sample, *M* to the middle sample, and *L* to the lower sample.

²The National Radio Astronomy Observatory is a facility of the National Science Foundation operated under cooperative agreement by Associated Universities, Inc.

For the first time we have a sample of microJy radio sources with nearly complete optical identifications and nearly 60% complete spectroscopic redshift measurements. Others are doing similar work on faint star forming radio galaxies (Hopkins et al. 1999; Mobasher et al. 1999; Benn et al. 1993; Gruppioni, Mignoli, & Zamorani 1999) with larger catalogs of sources. While our survey samples have fewer sources, we have generally more sensitive radio flux limits and more complete optical followup. In principle, this allows us to probe higher redshifts, and to increase the fraction of sources identified with star-forming galaxies (see §2.4).

2.2. Primary beam corrections

In each of the three radio surveys, the flux threshold varies significantly across the field due to the shape of the primary beam response of the VLA antennas. The flux limit listed in Table 1 is for the center of the field; the limiting flux S_{lim} increases to the edge of the field by about 1.5 for SSA13, and by about 10 for the larger HDF and V15 fields. To find the total surface density of sources n (the number of sources per angular area on sky), we determine the contribution of each source by considering the portion of the field in which that source could have been detected. Therefore, each source i contributes

$$B_i = \frac{1}{A_i(S_i, S_{lim})} \quad (1)$$

to the surface density of sources, where A_i is the solid angle on the sky in which the flux S_i of source i would be greater than the sensitivity limit of the radio survey S_{lim} . A faint source which could only be detected at the center of the field (small A_i) contributes more to the average surface density n than a strong source which could be detected over the entire primary beam area (large A_i). To determine A_i for each source, we used the shape of the VLA primary beam.³ The total surface density of sources for a survey is then

$$n = \Sigma B_i \quad (2)$$

Other instrumental effects that affect the point source sensitivity across the field, such as bandwidth smearing, time delay smearing, and geometrical smearing (Richards 2000), are negligible in the three VLA surveys. Pascarella et al. (1998) discuss the importance of surface brightness corrections in determining star formation history. However, the relatively low resolution of these radio surveys (3'' for the HDF and 3-10'' for the SSA13 and V15 fields), combined with the resolution correction as a function of flux density (Windhorst et al. 1990, 1993), suggests that few of these sources are resolved and thus no correction for surface brightness biases have been made.

³The gain of the VLA primary beam is well-matched by $g(r) = [\cos(\frac{-0.23226+74.567639r\nu}{57.2957795})]^6$ where r is the distance from the beam center in degrees and ν is the observing frequency in GHz (Oort & Windhorst 1985).

2.3. Redshifts

The redshifts for the sources in the sample are either spectroscopic measurements, estimates from I or HK'-band magnitudes, or random assignments (see Tables 1 through 4 and Figure 3). About 58% of the sources have spectroscopic redshifts. The highest spectroscopic redshift in the sample is a source at $z = 4.42$ in the HDF (Waddington et al. 1999); however, there is some evidence that this source may contain an AGN, so that its radio flux is not dominated by star formation (see §2.5 for how this source is treated in the calculations).

For 13% of the sources, approximate redshifts were found from I and HK' band magnitudes. Windhorst et al. (1994b) used Bruzual-Charlot models (1993) to find the dependence of I and HK' magnitude on redshift for milliJy radio sources; these models are plotted in Figure 2. When comparing these models with the 45 spectroscopic redshifts in our sample of fainter microJy radio sources, we found a significant dependence on radio flux density. We compensated by shifting the magnitude scale of these models to fit the I or HK' values of our sources that *do* have spectroscopic redshifts, with different shifts for different radio flux ranges (as listed in the caption of Figure 2). We then used the revised curves to estimate redshifts for our sources that have I or HK' band magnitudes but not spectroscopic redshifts. The resulting redshifts are crude, but are better than random assignments. We converted K magnitudes to HK' using $K = HK' - 0.3$ (Barger et al. 1999). The $I(z)$ model is double valued for $z \gtrsim 1$, and the $HK(z)$ model increases sharply for $z \gtrsim 3$, so when the I or HK' magnitude of a source indicated a redshift above these limits, we randomly assigned a redshift instead (see below).

For the remaining 29% of the sources, neither spectroscopic redshifts nor rough photometric redshifts were available. Rather than removing these sources from the sample, we assigned redshifts in the following manner. We first separated the sources into two groups: those with very faint ($I > 25$) or red ($I-K > 4$) optical identifications, and those with brighter optical identifications. The group with brighter identifications (10 sources) were assigned redshifts randomly selected from the list of spectroscopic redshifts of star-forming galaxies in the sample. The group with very faint or red optical identifications (12 sources) are probably star-forming galaxies at redshifts greater than 1 (Richards et al. 1999; Barger, Cowie, & Richards 2000). These sources were assigned redshifts randomly in the range $z = 1 - 3$.

The redshift distributions and total source densities of the three surveys are strikingly different (see Figure 3). The HDF and SSA13 surveys were both performed at 8 GHz with similar flux limits, yet the average source density (including all redshifts) is 1.3 sources/arcmin² in the HDF, but 2.7 sources/arcmin² in the SSA13 field, over twice as great. The total source density of the V15 field at 5 GHz is 0.7 sources/arcmin², which is nearly the same as the HDF field when the differences in flux limit and observing frequency are taken into account. The redshift distribution in the three fields peaks at somewhat different redshifts (see Figure 3), possibly due to galaxy superclustering or other high-redshift structure, although all three fields peak at $z < 1$ and have a long tail which extends to $z \sim 3$. The differences in the redshift distribution of the fields are probably due to

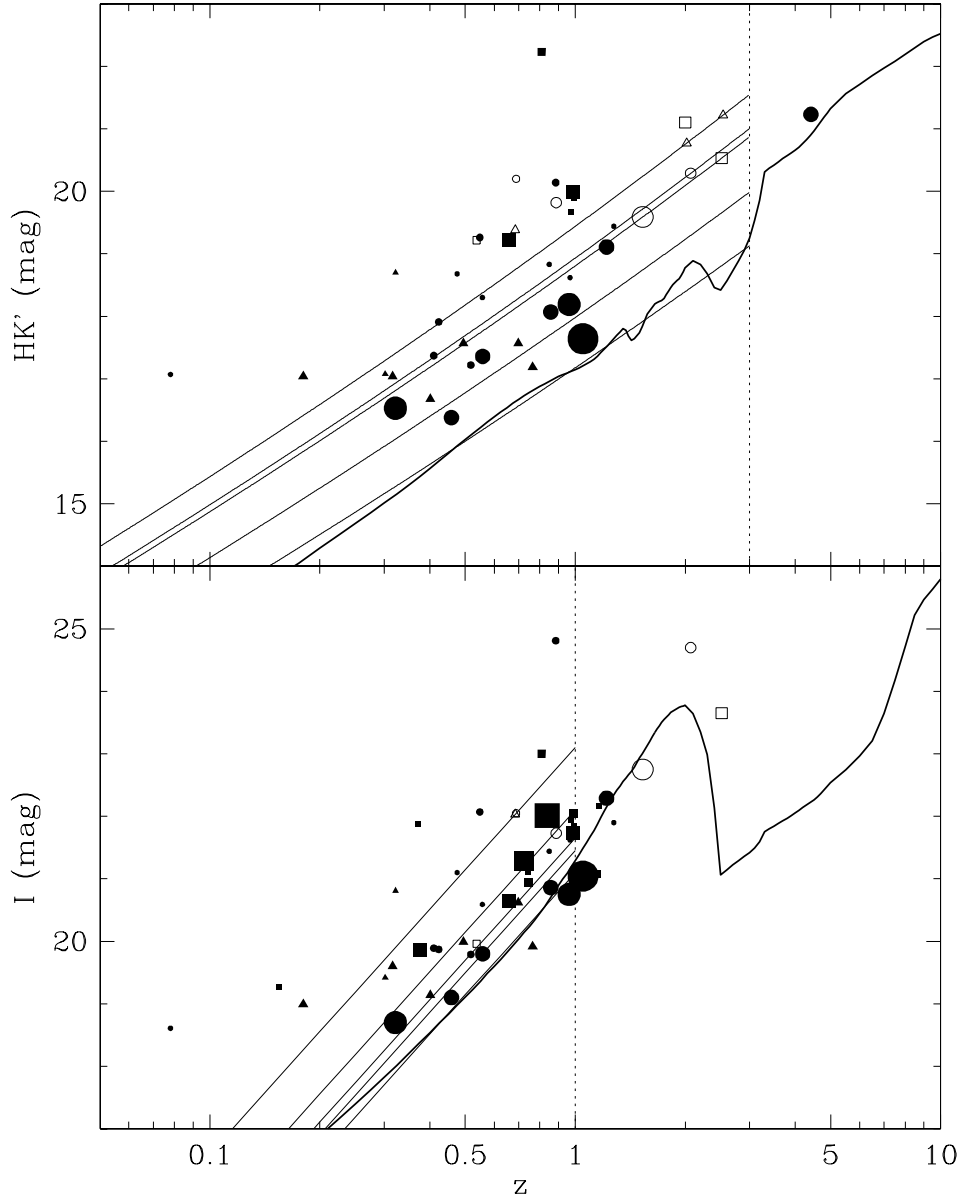


Fig. 2.— Estimation of photometric redshifts (see §2.3). Circles are sources in the HDF field, triangles in the SSA13 field, and squares in the V15 field. The symbol size is proportional to radio flux density. Solid symbols are spectroscopic redshifts, hollow symbols are photometric redshifts. The thick line is the model for the $I(z)$ and $HK'(z)$ relationships for faint radio sources (Windhorst et al. 1994b). The thin lines are parallel to the model curve, but are offset vertically to fit the spectroscopic redshifts in different radio flux density ranges. From bottom to top these flux ranges are: $S_8 > 300 \mu\text{Jy}$, $300 \mu\text{Jy} > S_8 > 100 \mu\text{Jy}$, $100 \mu\text{Jy} > S_8 > 30 \mu\text{Jy}$, $30 \mu\text{Jy} > S_8 > 18 \mu\text{Jy}$, and $S_8 < 18 \mu\text{Jy}$.

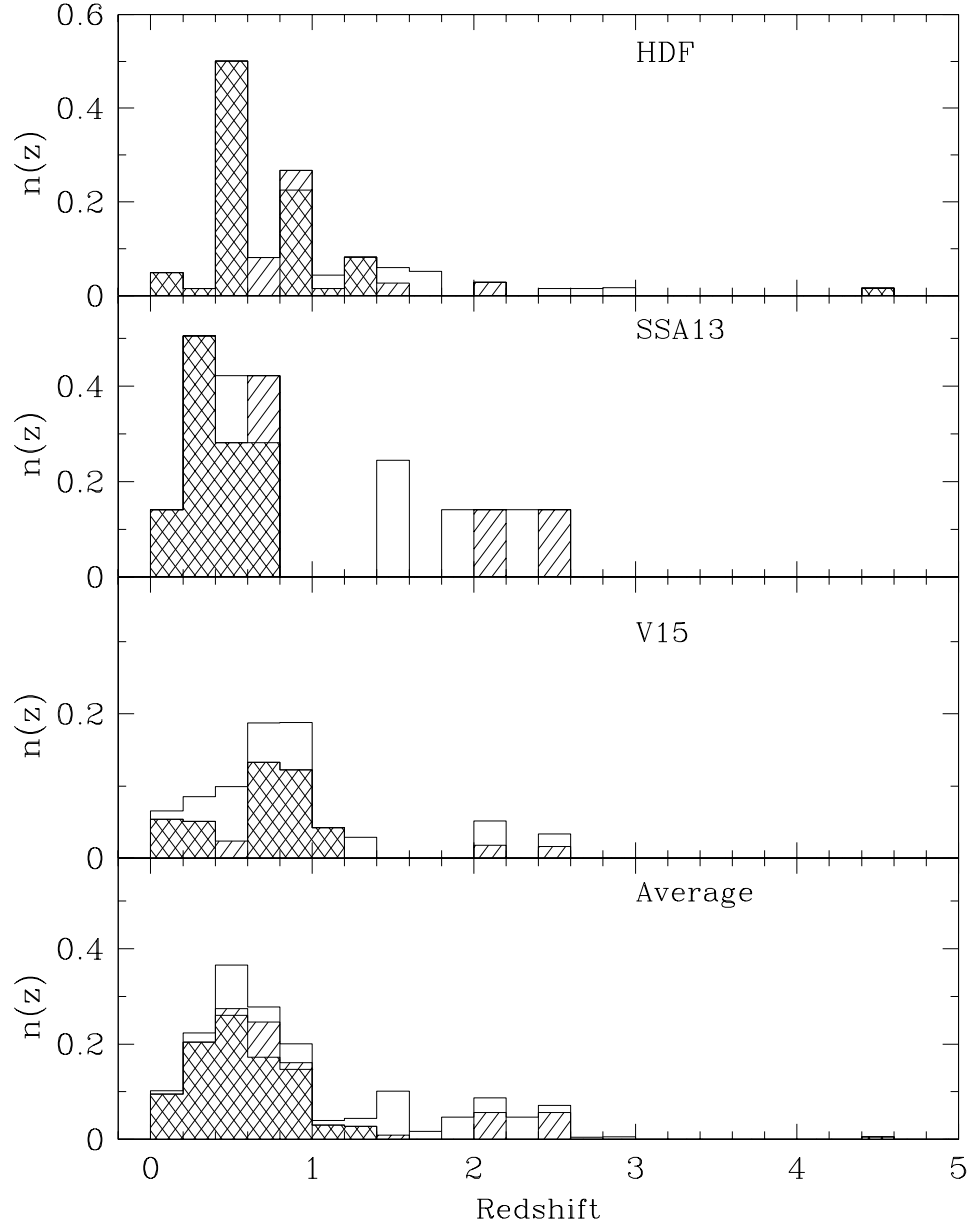


Fig. 3.— Redshift distribution of sources, in number/arcmin² and corrected for the primary beam (§2.2). Redshifts were measured spectroscopically (*cross-hash*), estimated from I- or HK'-band magnitudes (*hash*), or assigned (*blank*, see §2.3 for how assignments were made).

cosmic variance (note that each field is sampling only a small solid angle). Since these fields were generally chosen to be free of bright sources, the number counts may be too low in the HDF and V15 fields rather than too high in the SSA13 field (indeed, Richards 2000 reports a deficit of radio sources detected at 1.4 GHz in the HDF). To deal with the differences between fields, we average the three data sets together in our calculations.

2.4. Optical Identifications

Figure 4 indicates the nature of the available optical identifications of the radio sources. Known QSOs were removed from the sample (two from the SSA13 field, one from V15), as was one star in the V15 field and are not shown in the figure. For the remaining sources, the three fields appear to be significantly different. In the HDF, about 50% of the radio sources have star-forming counterparts (spirals, mergers, and irregulars; Richards et al. 1998), another 30% are in the red/optically faint category discussed above (several of which are identified with bright sub-mm objects and may include star-forming galaxies; Barger et al. 2000), and only 20% are identified with elliptical galaxies which presumably are associated with low luminosity AGN. In the SSA13 field, 50% are identified with star-forming or red/optically faint galaxies, and 50% are of unknown type. In the V15 field, 15% of the sources have unknown galaxy types, and 40% of the sources are likely to be star-forming or in the red/optically faint population (Hammer et al. 1995). A further 35% are claimed to be elliptical/AGN counterparts based on deep I-band images from the Canada-France Hawaii Telescope, and another 15% are classified by Hammer et al. as AGN based on emission line studies. Thus, Hammer et al. (1995) report a larger fraction of low-luminosity AGN in the V15 field (50%) than observed in the HDF (20%). However, HST/WFPC2 images of these identifications from the Groth Strip survey (Hammer 1996) show some ambiguity in the optical identifications, indicating a higher fraction of late type galaxies than originally reported by Hammer et al. (1995); thus some uncertainty remains. Also, the V15 field lies only 20 arcmin from the cluster associated with 3C295, and there is another supercluster or redshift structure at $z = 0.98$ within the field (Le Fevre et al. 1994). These structures have probably caused some bias in the identifications, increasing the fraction of early type radio galaxies. Thus we adopt the statistics from the HDF and SSA13 surveys, which imply that about 50% of the sources have disk or late type galaxy counterparts, 30% have red/optically faint identifications, and 20% are associated with ellipticals and low luminosity FR I type AGN.

2.5. Strategy for dealing with incomplete identifications and redshifts

The goal of this work is to calculate the global star formation history based on star-forming radio sources. Since not all of the sources are star-forming, and only 58% have spectroscopic redshifts, we must define the target population carefully. To do this, we separate the data into subsets in order to calculate lower and upper limits on the luminosity function and hence the star

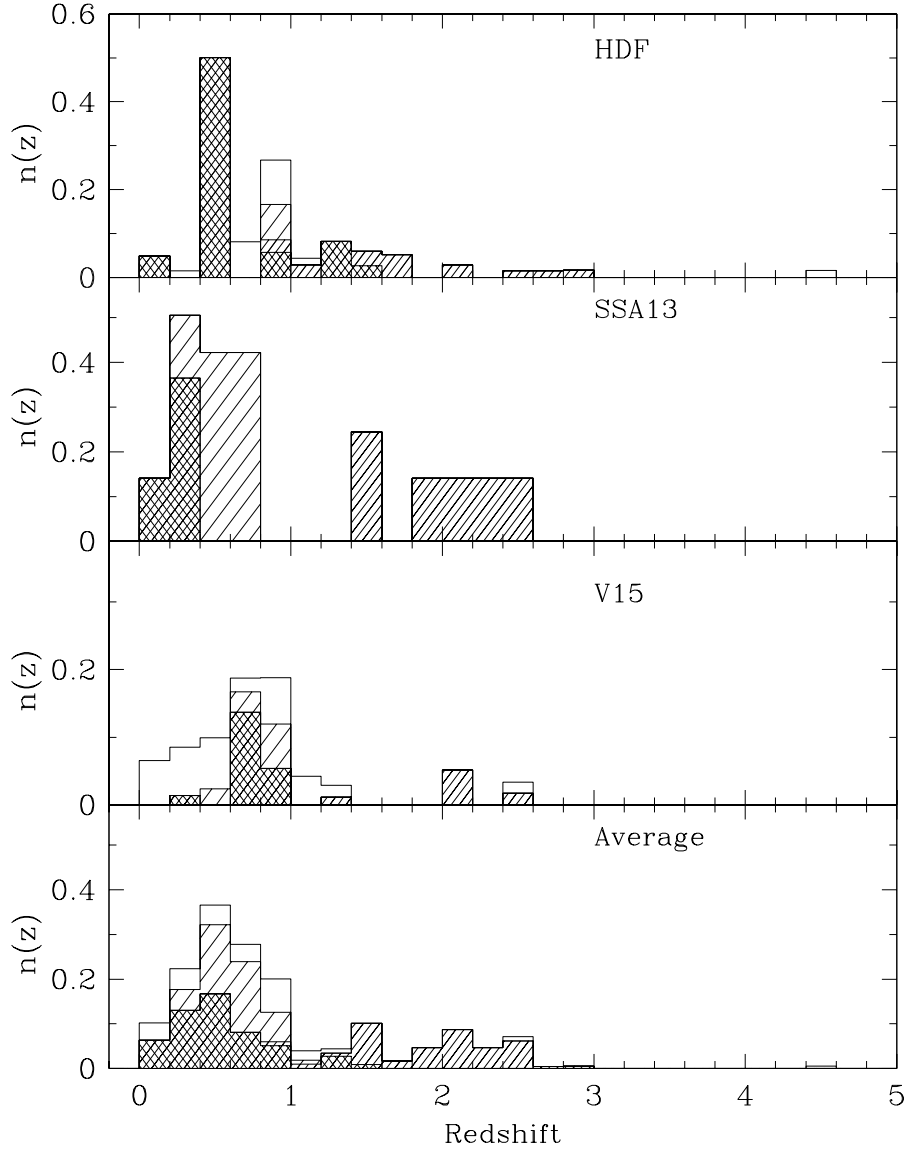


Fig. 4.— Redshift distribution of sources, *separated by galaxy type*, in number/arcmin² and corrected for the primary beam shape (§2.2). Indicated are spiral, irregular, or merging galaxies (*cross-hash*), very faint or red optical identifications (*narrow hash*), unknown or unclear identifications (*broad hash*), and elliptical or emission line galaxies (*blank*). Known QSOs and stars (just four sources in the three surveys) are not included in the figures or our calculations.

formation history (see Figure 5):

- a “lower limit” sample (23 sources): only those sources which are *both* identified with spiral/irr/mergers *and* have spectroscopic redshifts. These are the sources which definitely belong in the population of interest.
- a “middle value” sample (37 sources): only those sources for which two criteria are met:
 - redshift is spectroscopic *or* based on I- or HK'-band magnitude (no randomly assigned redshifts)
 - galaxy type is spiral/irr/merger, *or* faint/red. In addition, about 80% of the “unknown” identifications are assumed to be spiral/irr/merger or faint/red and are included here. The highest redshift source ($z = 4.42$ in the HDF) is not included here because Waddington et al. (1999) argue that it contains an AGN component.

This sample is our best estimate of the true redshift distribution of star-forming radio galaxies.

- an “upper limit” sample (all 77 sources): all sources (including identifications with elliptical, emission line, and a few Seyfert galaxies, but not verified QSOs which were removed from sample). Redshifts were assigned for those sources without spectroscopic or I- or HK'- band estimates. This sample shows the maximum star formation rate that the data would allow, assuming *all* radio flux from all detected sources is due to star formation and that the redshift estimates are correct.

3. Evolution of the luminosity function

Next we determine the evolution of the luminosity function for this population of faint star-forming radio galaxies, using the data described in §2. In §4.3 we will use this evolving luminosity function to build a model of the star formation history. Since our data contains very few low-redshift objects, we can not fit for the shape of the local luminosity function. Instead, we use the local luminosity function found by Condon (1989), and fit for the evolution of that function in luminosity and number density. In §3.1 we calculate the luminosity function directly from the data, in §3.2 we describe the evolution model, and in §3.3 we describe the observational constraints on that model and the resulting best fit.

We convert all observed luminosities to a rest-frame frequency of 1.4 GHz, since most of the work on the local luminosity function has been done at this frequency. Our samples are defined at 5 and 8 GHz, but some sources have also been detected at 1.4 GHz. We use the observed 1.4 GHz flux densities when available, and for the remaining sources we assume a spectral index of $\alpha = 0.4$ (see §1) to convert to 1.4 GHz, unless this violates an observed limit on the 1.4 GHz flux density. All source luminosities are then converted from the observed 1.4 GHz value to their rest-frame

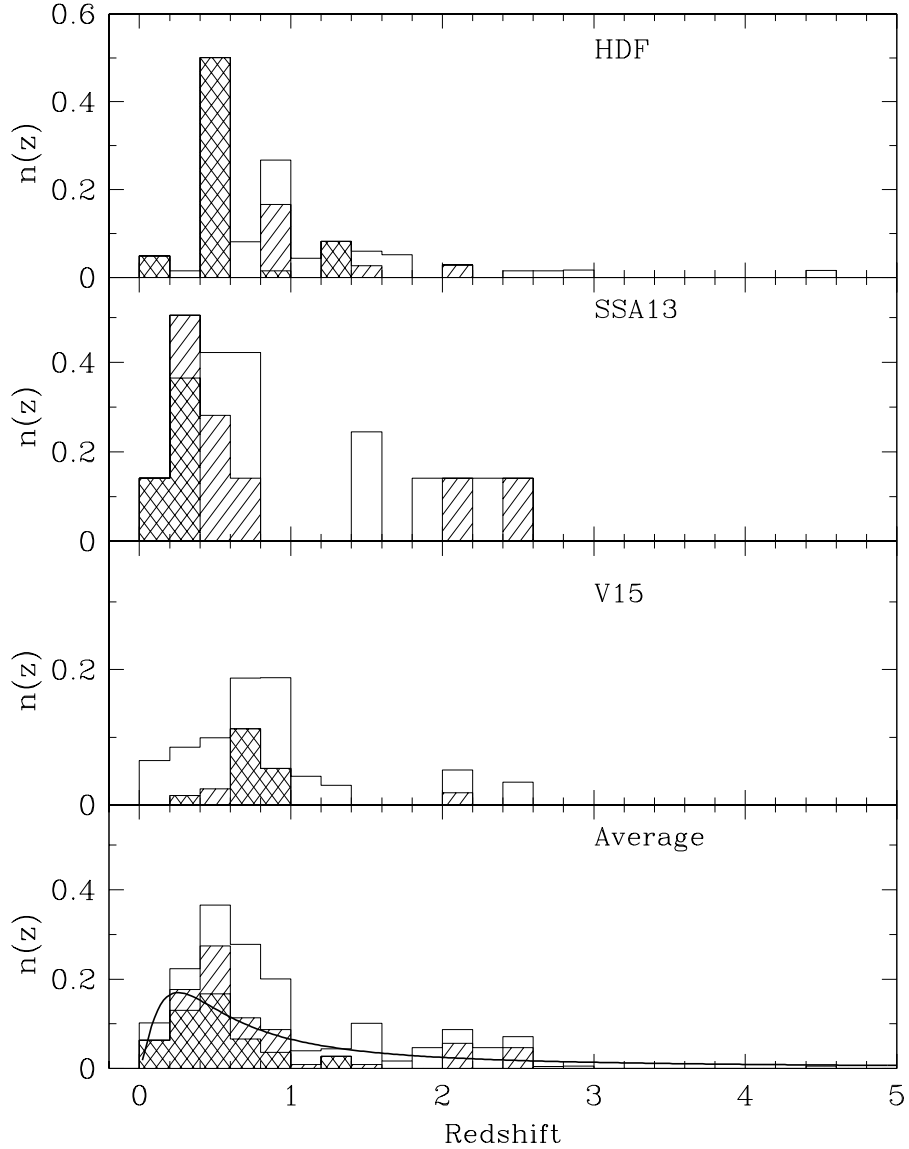


Fig. 5.— Redshift distribution of sources, separated into the “lower” sample (*cross-hash*), “middle” sample (*cross-hash and hash*), and “upper” sample (*all sources shown*). These samples are used in §3 and §4 to calculate a “middle” value with lower and upper limits; see §2.5 for how samples are defined. The curve is the model prediction based on a fit to the middle sample shown here and other data (see discussion in §3.3).

1.4 GHz value. Thus, the observed luminosity of each galaxy $L_{o,\nu}$ at an observing frequency ν and redshift z , is converted to the emitted luminosity at 1.4 GHz rest-frame frequency using

$$L_{e,1.4} = L_{o,\nu} \left(\frac{\nu}{1.4 \text{ GHz}} \right)^\alpha (1+z)^\alpha \quad (3)$$

We define the luminosity function $\phi(L_{e,1.4})$ as the number per comoving Mpc^3 per $d \log_{10} L$ of star-forming radio sources with emitted luminosity $L_{e,1.4}(\text{W/Hz})$ at 1.4 GHz.

3.1. Luminosity function estimated from the data

We can calculate the luminosity function directly from the detected sources for those luminosity and redshift ranges which are sampled by the data sets described in §2. For each bin in luminosity ($L_{min} < L_{e,1.4} < L_{max}$) and redshift ($z_{min} < z < z_{max}$), the luminosity function is

$$\phi(L_{e,1.4}, z) d \log_{10} L = \Sigma_i \frac{B_i}{V_c[z_{min}, z_{max}(L_i)]} \quad (4)$$

where B_i is the surface density, corrected for the primary beam (eq. 1), and $z_{max}(L_i)$ is the largest z in the bin for which the luminosity of the source L_i was above detection limit of survey. V_c is the comoving volume (in Mpc^3) between z_{min} and z_{max} for solid angle $\Delta\Omega$,

$$\begin{aligned} V_c(z_{min}, z_{max}, \Delta\Omega) &= \int d\Omega \int r^2(z) dr \\ &= \frac{\Delta\Omega}{\text{ster}} \left(\frac{\text{ster}}{1.18 \times 10^7 \text{ arcmin}^2} \right) \frac{[r^3(z_{max}) - r^3(z_{min})]}{3}, \end{aligned} \quad (5)$$

where the comoving distance is

$$r(z) = \frac{2c}{H_0} \left(1 - \frac{1}{\sqrt{1+z}} \right) \quad (6)$$

for our assumed cosmology (see §1).

The binned luminosity function was calculated using eq. 4 for the lower, middle, and upper samples described in §2.5, using the average of the three surveys (bottom panel of Fig. 5). The result is shown in Figure 6, where the data points are from the “middle” sample, and are plotted at the average of the luminosities in each bin. Vertical error bars are either the lower and upper limits (from the samples described in §2.5), or the Poisson errors ($1/\sqrt{N}$ weights from the number of galaxies per bin), whichever is larger (generally the Poisson errors dominate for the low redshift data, and the lower/upper sample limits dominate for the high redshift data). Horizontal error bars are the range of source luminosities in each bin. Bins were chosen such that each contains 4 to 6 galaxies (except for the lowest redshift bin which has only 2 galaxies).

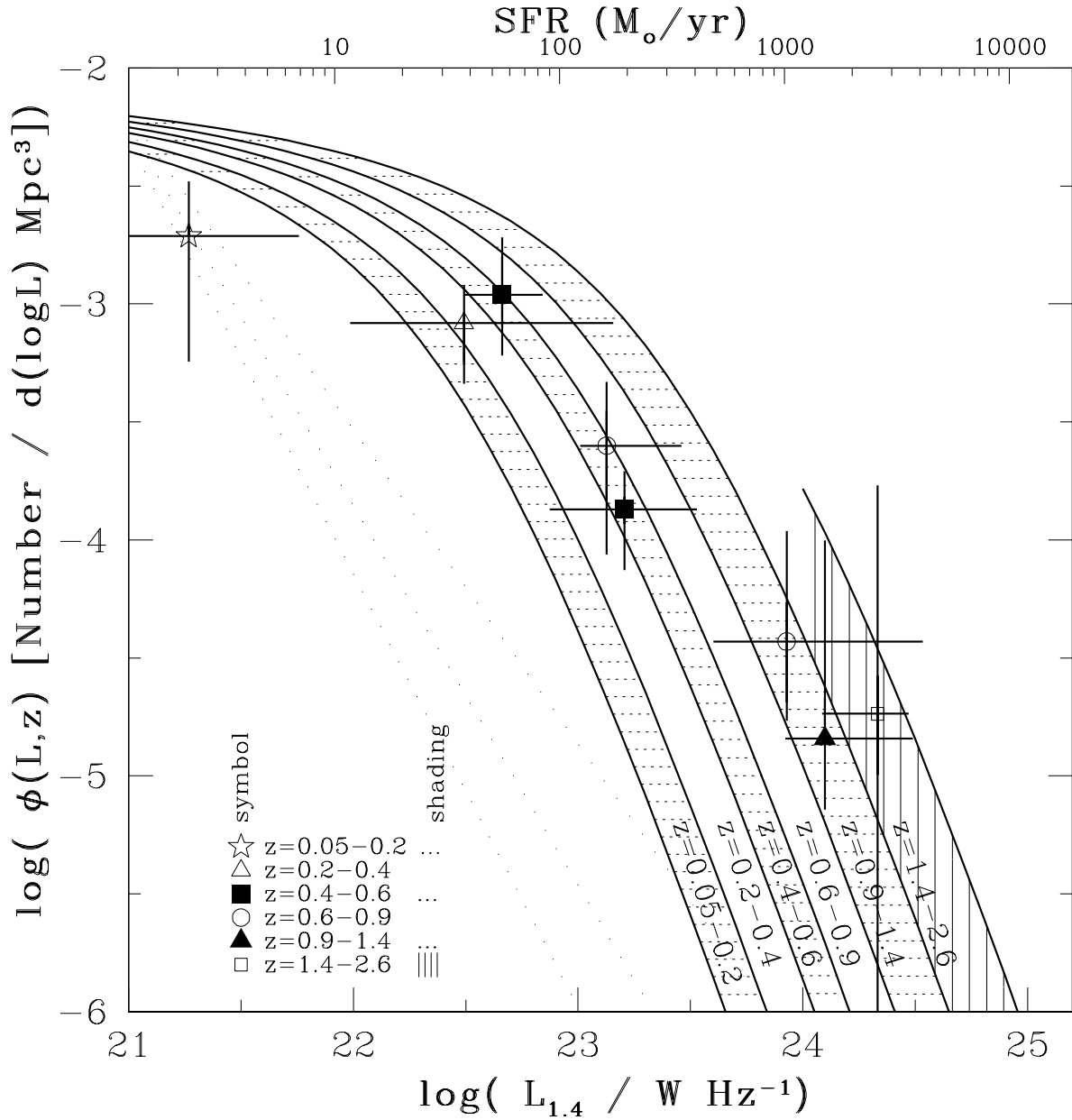


Fig. 6.— Evolving luminosity function for faint star-forming radio sources. Data points are averaged over the three surveys. Symbol shapes and shading correspond to the redshift ranges indicated. Horizontal error bars indicate the range of source luminosities in the bin. Vertical error bars are the larger of the Poisson errors or the lower/upper limits (see §3.1). The curves are the model evolving luminosity function, found from a fit to these and other data (see discussion in §3.3).

3.2. Description of evolving luminosity function model

We now build a model of the evolving luminosity function in order to compare it to several observables. In §3.3 we describe the observational constraints, the fitting process, and the resulting fit of this model to the observed data. Here we describe the model and its free parameters.

We use the local 1.4 GHz luminosity function for star-forming/spiral galaxies from Condon (1989, eq. 8 and discussion after eq. 7), adopting different notation,

$$\log_{10}[\phi(L_{e,1.4})]d\log_{10} L = 28.83 + Y - 1.5\log_{10} L_{e,1.4} - \left[B^2 + \frac{1}{W^2}(\log_{10} L_{e,1.4} - X)^2 \right]^{1/2} d\log_{10} L, \quad (7)$$

with the fitted parameters for star-forming galaxies of $Y = 2.88$, $X = 22.40$, $W = 2/3$, and $B = 1.5$. The factor of 28.83 includes unit conversions and the conversion from magnitudes ($d\log_{2.5} L$) to base 10 ($d\log_{10} L$).

To describe the evolution of the luminosity function, we use the functional form suggested by Condon (1984b, eq. 24), a power-law in $(1+z)$ with an exponential cut-off at high redshift. The luminosity evolves as

$$f(z) = (1+z)^Q \exp \left[- \left(\frac{z}{z_q} \right)^q \right], \quad (8)$$

and the number density evolves as

$$g(z) = (1+z)^P \exp \left[- \left(\frac{z}{z_p} \right)^p \right]. \quad (9)$$

This gives six free parameters $\{Q, q, z_q, P, p, z_p\}$ to use in describing the evolution. Thus the general expression for the evolving luminosity function is (Condon 1984a)

$$\phi(L_{e,1.4}, z) = g(z) \phi \left(\frac{L_{e,1.4}}{f(z)}, 0 \right). \quad (10)$$

Once we know the evolving luminosity function, it can be used to predict the observed redshift distribution, $n(z)$. The number of sources between z_{min} and z_{max} that could be detected in a survey of angular area $\Delta\Omega$ and flux limit S_{lim} at frequency ν is

$$n(z) = V_c(z_{min}, z_{max}, \Delta\Omega) \int_{L'(S_{lim}, z)}^{\inf} \phi(L_{e,1.4}, z) d\log_{10} L \quad (11)$$

where the lower limit of the integral is the luminosity corresponding to the flux limit S_{lim} at the redshift z . The comoving volume V_c is defined in eq. 5.

The evolving luminosity function can also be used to predict the extragalactic background due to this population. The background intensity at observing frequency ν_0 is (Dwek et al. 1998)

$$I(\nu_0) = \frac{1}{4\pi} \int \rho(\nu, z) \left| \frac{cdt}{dz} \right| dz \quad (12)$$

where the luminosity density, ρ , emitted at redshift z and frequency ν is found from the luminosity function,

$$\rho(\nu, z) = \int L_{e,1.4} \phi(L_{e,1.4}, z) d \log_{10} L, \quad (13)$$

and

$$\left| \frac{dt}{dz} \right| = \frac{1}{H_0(1+z)^{5/2}} \quad (14)$$

for the assumed cosmology (§1).

3.3. Fitting the evolving luminosity function model to the data

We can now compare the evolution model to the observed data in order to fit for the evolution parameters. The model is constrained by three observables:

1. The redshift distribution, $n(z)$. We use the “middle” sample (defined in §2.5) for the average of three surveys, shown as the hashed area in the bottom panel of Figure 5.
2. The observed luminosity function, shown as the data points in Figure 6. We use the error bars shown in the figure (the larger of lower/upper limits and Poisson errors).
3. The extragalactic radio background, which is an important constraint on the integral of the luminosity function.

The first two constraints are not independent from each other, but both are needed. In order for the observed luminosity function to have 4-6 sources per bin, only coarse redshift resolution is possible; the $n(z)$ distribution allows for more detailed redshift information, but does not include the luminosity information.

The extragalactic radio background is about half due to star-formation activity and half due to AGN (see discussion in Haarsma & Partridge 1998). In order to isolate the part of the radio background due to star formation, we use the far-infrared (FIR) background found by DIRBE of $1.15 \pm 0.20 \times 10^{-20} \text{ Wm}^{-2}\text{ster}^{-1}\text{Hz}^{-1}$ near $200 \mu\text{m}$ (Hauser et al. 1998), assumed to be due primarily to star formation. The FIR-radio correlation (Helou, Soifer, & Rowan-Robinson 1985; Condon, Anderson, & Helou 1991) can then be used to predict the portion of the radio background due to star-formation, which at 1.4 GHz is $\rho = 3.2 \pm 0.6 \times 10^{-23} \text{ Wm}^{-2}\text{ster}^{-1}\text{Hz}^{-1}$.

For each trial set of evolution parameters $\{Q, q, z_q, P, p, z_p\}$, we calculate the model prediction for $n(z)$, the evolving luminosity function, and the radio background due to star formation. The evolution parameters are adjusted to improve the model fit to the three data constraints, using a downhill simplex algorithm (Press et al. 1992) to find the global χ^2 minimum. Since the $n(z)$ and luminosity function constraints are not independent from each other, the reduced χ^2 can not be

used to calculate the “goodness of fit” or to quantitatively compare the quality of different fits, but its minimum still indicates the parameters of the best available fit.

Our best fit is $\{Q = 3.97, q = 1.02, z_q = 1.39, P = -0.0579, p = 23.1, z_p = 14.3\}$. The resulting evolution factors $f(z)$ and $g(z)$ are plotted in Figure 7. The $n(z)$ distribution predicted by the model is shown in Figure 5 (bottom panel). The peak of the model $n(z)$ distribution falls at a lower redshift ($z \sim 0.3$) than the peak in the data ($z \sim 0.5$), but the tail of the distribution is reasonable and the total number density under the curve is similar (within 5%) for the data and the model (models with a peak at higher redshift tend to have a much shorter tail or a larger total number of sources n and thus a larger discrepancy with the observed total). The luminosity function predicted by the model is shown as the curves in Figure 6, and is a good fit to the data points, except for the $z = 0.05 - 0.2$ bin (which includes only two galaxies), and the $z = 0.6 - 0.9$ bin (where one point is too high and the other is too low). The model predicted star-forming radio background is $3.0 \times 10^{-23} \text{ Wm}^{-2}\text{ster}^{-1}\text{Hz}^{-1}$, which is a reasonable fit to the observed value. While the model does not perfectly match the three data constraints, it is the best compromise between them. Models that give a better fit to the observed $n(z)$ shape result in a poor fit to the other two data constraints. For instance, some evolution models can produce a longer tail on the $n(z)$ distribution, but that raises the total background and the total surface density n significantly above the observed levels.

In the early stages of this work, it seemed that the full 6 parameters of our evolution model (eqs. 8, 9) were necessary to achieve a good fit. In the end, the best fit model shows virtually no number density evolution, and only a mild turn-over in luminosity evolution. Pure luminosity evolution $\{i.e. f(z) = (1 + z)^Q \text{ and } g(z) = 1\}$ has often been suggested in the literature (Rowan-Robinson et al. 1993; Hopkins et al. 1998). It turns out that pure luminosity evolution with $Q = 2.74$ gives a similar fit to the luminosity function data points, but predicts a tail on the $n(z)$ distribution which extends beyond $z = 5$, and a star-forming radio background that is slightly too high ($4.1 \times 10^{-23} \text{ Wm}^{-2}\text{ster}^{-1}\text{Hz}^{-1}$).

The 6 parameters used here are very interdependent. As we progressed through this work, adding data and model features, we fit our model to the data numerous times. The resulting fits occurred in a wide range of this parameter space, with the turnover at high redshift sometimes occurring in $f(z)$ (luminosity evolution) and sometimes occurring in $g(z)$ (number density evolution). Some fits had a steeper increase in $f(z)$ and a decrease in $g(z)$, others had a shallower increase in $f(z)$ and an increase in $g(z)$. This reminds us that the 6 parameters are degenerate, and most likely a different parameterization with fewer free parameters could describe the data as well. Finding a new parameterization, however, would go beyond the scope of this present work, given the limited sample size currently available. Although the shapes of $f(z)$ and $g(z)$ varied greatly between different fits, all of the fits predicted generally similar shapes for the observables (the $n(z)$ distribution and the luminosity function), and for the predicted global star formation history (see §4.3).

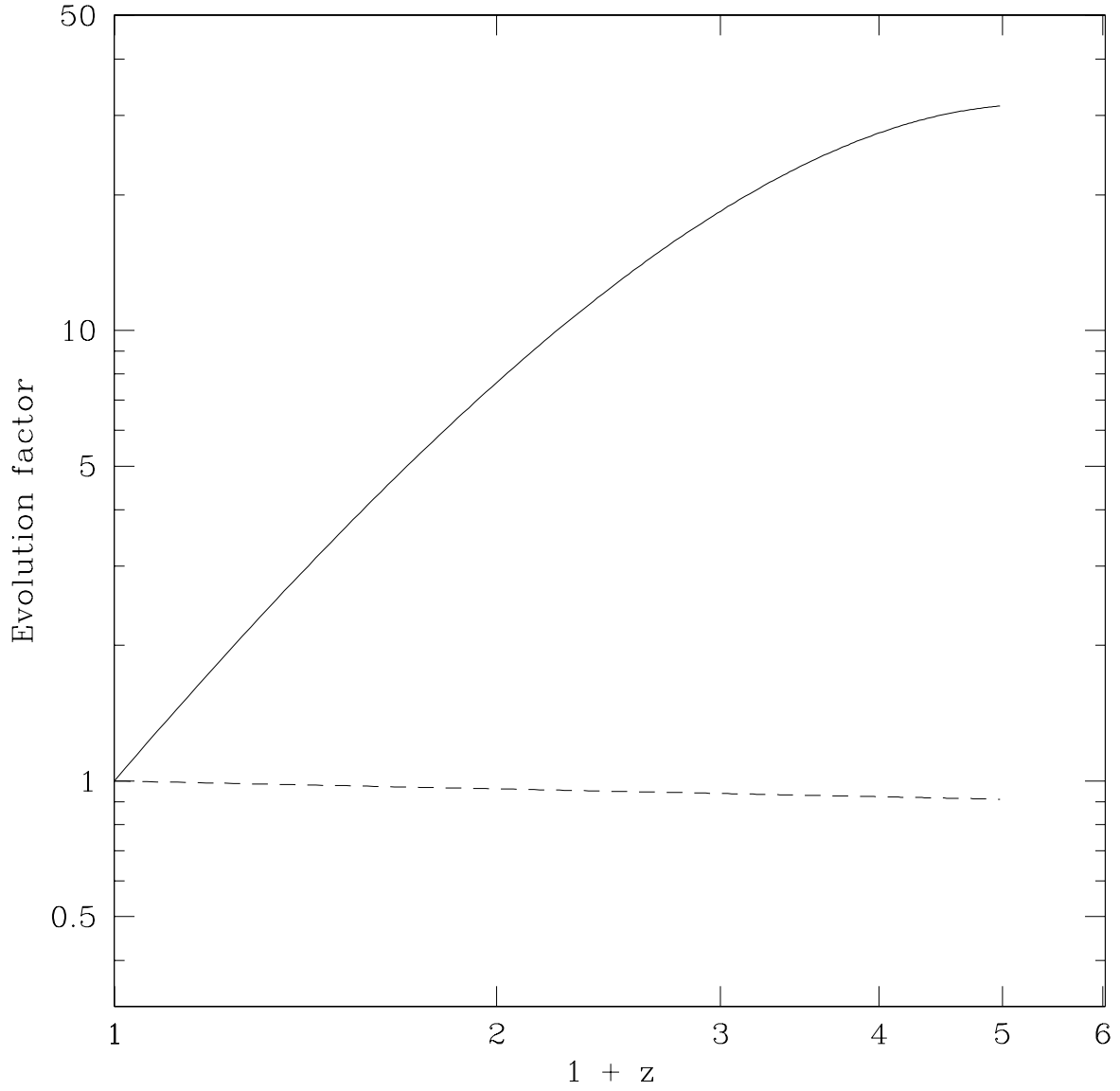


Fig. 7.— Evolution functions for the fitted model found in §3.3. The solid line is $f(z)$ (luminosity evolution), and the dashed line is $g(z)$ (number density evolution) (see eqs. 8 and 9).

4. Star Formation History

Now that we have a model of the evolving luminosity function, we can use it to determine the star formation history. First we describe the relationship between star formation rate and radio luminosity (§4.1), then calculate the star formation history directly from the data with minimal model dependence (§4.2), and finally calculate it from the model (§4.3).

4.1. Star formation rate from radio luminosity

For an individual star-forming galaxy, the star formation rate is directly proportional to its radio luminosity (Condon 1992):

$$\text{SFR} = Q \left(\frac{L_\nu / (\text{WHz}^{-1})}{5.3 \times 10^{21} (\nu / \text{GHz})^{-0.8} + 5.5 \times 10^{20} (\nu / \text{GHz})^{-0.1}} \right) M_\odot \text{yr}^{-1} \quad (15)$$

Condon (1992) derives this relation by calculating the synchrotron radio emission from supernova remnants (the first term in the denominator) and the thermal radio emission from HII regions (the second term). The spectral index of 0.8 is typical for the non-thermal component of a radio source at 1.4 GHz. This relation is derived purely from radio considerations. Cram et al. (1998), however, compares this relation to H α studies, and finds that they give similar star formation rates for local individual galaxies, with the exception of galaxies with extremely large star formation rates. (Hopkins et al. 2000 has found SFR-dependent dust corrections that shift the optical results to match 15 and radio observations.)

Both the thermal and non-thermal components of the radio expression are proportional to the formation rate of high-mass stars ($M > 5M_\odot$) which produce supernova and large HII regions, so the factor Q is included to account for the mass of *all* stars in the interval $0.1 - 100M_\odot$,

$$Q = \frac{\int_{0.1M_\odot}^{100M_\odot} M\psi(M)dM}{\int_{5M_\odot}^{100M_\odot} M\psi(M)dM}, \quad (16)$$

where $\psi(M) \propto M^{-x}$ is the initial mass function (IMF). We have assumed throughout a Salpeter IMF ($x = 2.35$), for which $Q = 5.5$. If an upper limit of $125M_\odot$ is used, then $Q = 5.4$. If we use a range of mass $0.25 - 100M_\odot$, as suggested by Gould, Bahcall, & Flynn (1996) then $Q = 3.9$. We will use $Q = 5.5$ in the following.

Condon’s relationship (eq. 15) uses the emitted source luminosity at a frequency of 1.4 GHz, and thus the corrections given in eq. 3 must be applied. We should also consider whether there are other ways in which the connection between SFR and radio luminosity might evolve with redshift. At 1.4 GHz, the thermal term in eq. 15 is much smaller than the synchrotron term, so evolution in the thermal term will have little effect. In the synchrotron term, the dependence of the emitted flux on the supernova environment is weak (Condon 1992), so little evolution is expected. However,

at high redshifts, relativistic electrons may experience significant inverse-Compton cooling from the intense FIR energy density or the cosmic microwave background. Another effect that might cause significant evolution in eq. 15 is an evolving IMF, entering through the factor Q . In active starbursts, the IMF may be weighted to high-mass stars (Elmegreen 1999), which would result in a smaller value of Q . However, the smallest Q is unity (when virtually all mass occurs in high-mass stars), so the strongest decrease in our calculated star formation history from a radical change in the IMF would be roughly a factor of five. Note that evolution of the IMF would affect optical estimates of the star formation rate as well. In the following calculations we assume that eq. 15 does not evolve.

To determine the star formation rate per comoving volume, we simply substitute the radio luminosity density (such as eq. 13 or 18) for the source luminosity L_ν in eq. 15, giving

$$\Psi(z) = Q \left(\frac{\rho_{e,1.4}(z)}{4.6 \times 10^{21} \text{ WHz}^{-1} \text{ Mpc}^{-3}} \right) \text{ M}_{\odot} \text{ yr}^{-1} \text{ Mpc}^{-3} \quad (17)$$

where 1.4 GHz is used in the denominator of eq. 15, as all data have already been converted to 1.4 GHz in the rest frame.

4.2. Star formation history estimated from the data

We now calculate the star formation history directly from the survey data in §2 by using the luminosity density of the detected sources. For each redshift bin ($z_{min} < z < z_{max}$), the luminosity density is

$$\rho_{e,1.4}(z) = \sum_i \frac{L_i B_i C(z)}{V_c(z_{min}, z_{max}(L_i))} \quad (18)$$

where B_i is the surface density given in eq. 1, $C(z)$ is a correction for faint sources described below, $z_{max}(L_i)$ is the largest z in the bin for which the luminosity of the source L_i was above detection limit of survey, and V_c is the comoving volume given in eq. 5. This luminosity density can then be used in eq. 17 to find the evolving star formation density. Without the correction factor $C(z)$, the luminosity density includes only individual sources brighter than the flux limit of the survey. It does not include the luminosity density of sources too faint to be detected individually, and so it clearly underestimates the star formation rate (but calculations without $C(z)$ have the advantage of being independent of our evolution model and provide a lower limit).

To account for these faint sources, we use the evolving luminosity function found in §3.3. Figure 8 illustrates the faint source correction, using a redshift of 1.6 as an example. The integral under the curve in the figure is proportional to the total luminosity density. The flux limit of the survey, however, only allows detection of individual sources above a certain luminosity, *i.e.* in the cross-hatch area. The faint source correction factor $C(z)$ in eq. 18 would then be the ratio of the total area to the cross-hatch area. We have argued, however, that the slope of the source number counts changes below about $1 \mu\text{Jy}$ (Haarsma & Partridge 1998), so that in fact most of the sources

will occupy only the hashed area of fig. 8. Thus, a more realistic correction to eq. 18 is the ratio of the hashed region to the cross-hashed region, *i.e.* the ratio of the luminosity density due to sources brighter than $1 \mu\text{Jy}$ to the luminosity density from sources brighter than the flux limit of the survey,

$$C(z) = \frac{\int_{L(S_{lim},z)}^{\text{inf}} L_{e,1.4} \phi(L_{e,1.4}, z) d \log_{10} L}{\int_{L(1 \mu\text{Jy},z)}^{\text{inf}} L_{e,1.4} \phi(L_{e,1.4}, z) d \log_{10} L} \quad (19)$$

A list of corrections for several redshifts is given in Table 5. Note that if the slope of the number counts of radio sources were assumed to stay the same below $1 \mu\text{Jy}$, these corrections would be even larger, and so would the calculated star formation density.

We calculated the star formation density using eqs. 17, 18, 19 for the lower, middle, and upper samples described in §2.5; the results are shown in Figures 9 and 10 and listed in Table 6. Recall that the “lower” sample includes only sources with spectroscopic redshifts and definite identifications with spirals, irregulars, or mergers, and thus is the minimum amount of star formation activity consistent with the data. The “middle” value includes some sources with ambiguous identifications and rough photometric redshifts, but is our best guess at the total radio-selected star-forming population. The “upper” sample includes all the sources and is the maximum possible star formation activity allowed by the radio data. In Figure 9, the points are values calculated from the middle sample, plotted at the average of the source redshifts in the bin. The vertical error bars are either the limits from the lower and upper samples, or the Poisson errors (from the number of galaxies per bin), whichever is larger (in most cases, the lower limits and upper limits are larger than the Poisson errors). To make the lower sample a true lower limit, we did *not include* the faint source correction $C(z)$. Thus the lower limit is for only those sources clearly identified with star forming systems *and* having spectroscopic redshifts, with no allowance made for evolution of the luminosity function or for sources below the survey flux limits. This is surely a gross underestimate of the true star formation density value, since faint sources, unidentified sources, and sources without spectroscopic redshifts are all missing, but it provides a firm lower limit to the true star-formation rate. The “middle” and “upper” samples do have the correction $C(z)$ for faint sources applied.

Mobasher et al. (1999) have done a similar calculation of star formation density from a survey of faint radio sources. They find no evidence for evolution from $z = 0$ to $z = 1$, and a *decrease* in star formation density above $z = 0.3$. Their results, however, are based on a radio survey sample that is only 50% complete, and thus their results are highly dependent on assumptions made when correcting for incompleteness. Similarly, their optical identifications and spectroscopic redshifts are much less complete than ours. Finally, the radio surveys we use extend to much fainter flux densities where star formation is more likely to dominate the radio emission. The fainter flux limit also allows us to detect more high redshift sources. Thus, we believe our results for the star formation density are more reliable than those of Mobasher et al. (1999).

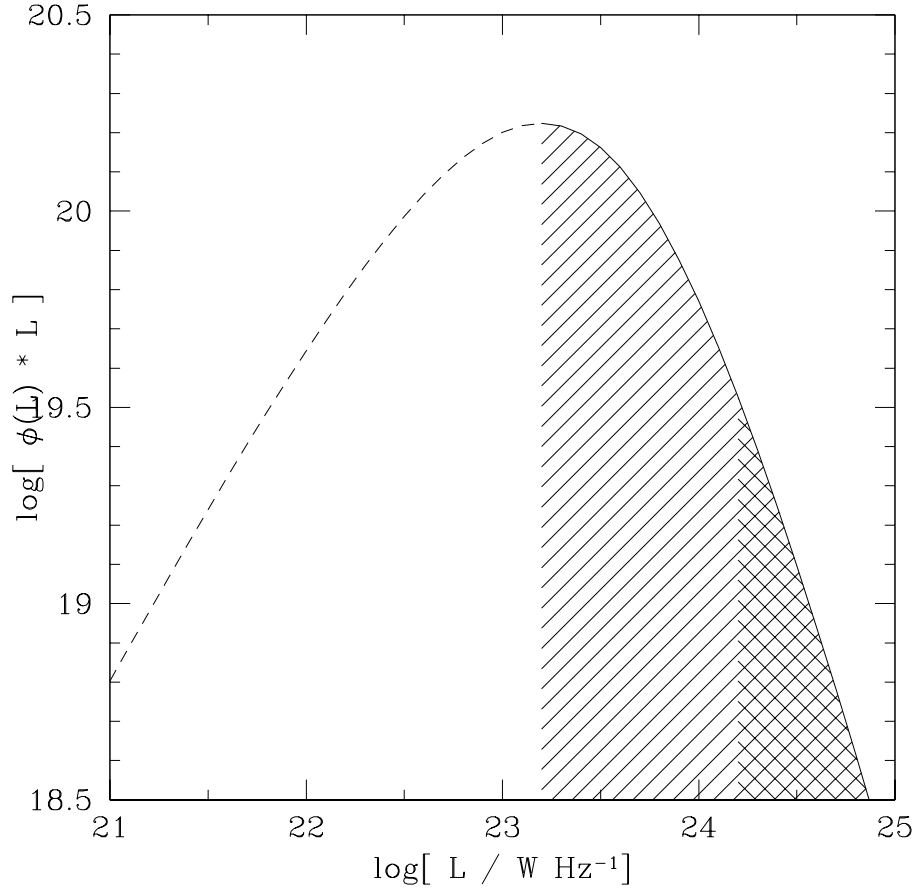


Fig. 8.— The integral under the $\phi(L) * L$ curve is proportional to the luminosity density. The relation for redshift $z = 1.6$ is shown. The total luminosity density is due to all sources brighter than $S_{8 \text{ GHz}} \sim 1 \mu\text{Jy}$ (*hash*), but only discrete sources above $S_{8 \text{ GHz}} \sim 9 \mu\text{Jy}$ are detected in the survey sample (*cross-hash*). The ratio of the two regions gives the correction to the luminosity density needed to account for sources too faint to be detected individually in the survey; here it is about 3.8.

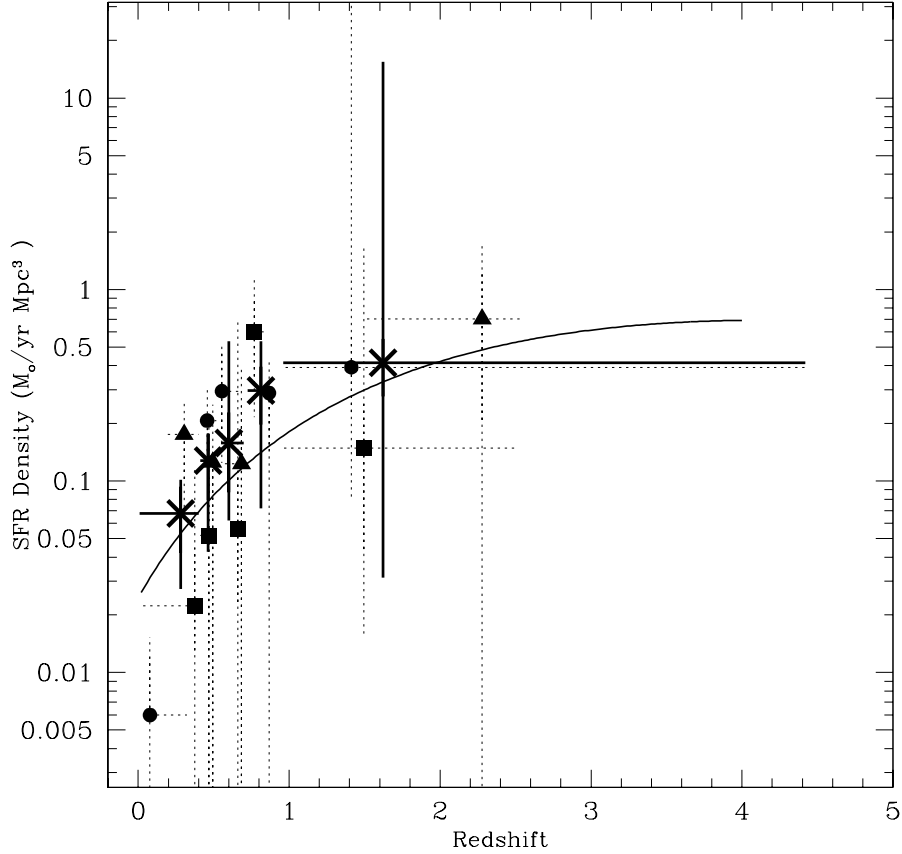


Fig. 9.— Star formation history data points (see §4.2). Circles are from the HDF field, triangles from the SSA13 field, and squares from the V15 field. The average is shown with crosses and solid error bars. The curve is the star formation history predicted by the model evolving luminosity function (note that this curve was *not* fit to the data points shown here, see §4.3). Vertical error bars are the larger of Poisson errors or lower/upper limits (§2.5). Horizontal error bars are the range of source redshifts in the “upper” sample.

4.3. Star formation history predicted by model

The star formation history can also be determined directly from the evolution model found in §3.3. We simply calculate the luminosity density emitted at 1.4 GHz (eq. 13), and use eq. 17 to find the star formation density. The resulting star formation density prediction is the curve plotted in Figures 9 and 10.

The model curve in Figures 9 and 10 falls somewhat below the averaged data points (heavy crosses). Note that the model curve was *not* fitted to these averaged data points (which were calculated using equations 17, 18, 19), but rather the model was found from the evolving luminosity function alone (using equations 13 and 17). The evolving luminosity function, in turn, was fitted to the $n(z)$ data, the luminosity function data, and the radio background (see §3.3). As discussed in §3.3, our model fits these data well but not perfectly, so small differences between the model prediction and the star formation data points are not unreasonable.

This sort of calculation was previously done by Cram (1998), using the Condon (1989) luminosity function and Condon (1984a) evolution model. Please note the typographical error in eq. 2 of Cram (1998), which differs by a factor of 28.2 from our eq. 15; the correct values were used in their calculations (L. Cram, private communication). We agree with Cram’s calculation of $0.026 \text{ M}_{\odot} \text{ yr}^{-1} \text{ Mpc}^{-3}$ for the local star formation density, and calculation of star formation history from Condon’s early model.

Note that these methods and results are much improved over our very preliminary work (Haarsma & Partridge 1999), which assumed that the majority of detected faint radio sources lie at the redshift of peak star formation activity. In fact, the peak of the observed redshift distribution (Figures 3-5) is at a lower redshift than the peak star formation activity (Figures 9 and 10), due to cosmological factors, such as the dependence of the comoving volume on redshift.

5. Discussion and Conclusions

Radio wavelength determinations of the Universal star formation history have the important advantage of being independent of the dust content of galaxies. Additionally, it is possible to cull relatively clean samples of star-forming objects using radio properties such as spectral index, morphology, and variability. Our results are shown in Figure 10, overlaid with the star formation histories found in several other studies. In Figure 10, the thick crosses show the star formation density of our middle sample, with error bars indicating Poisson errors. Although it is possible that our middle sample may include some low-luminosity AGN (Seyferts, etc.), our careful definition of the sample (§2.5) and the large fraction of sources with clear optical identifications reduces this contamination. The thin curve is our model prediction, found in §4.3 by fitting to the luminosity function, redshift distribution, and radio background (not to the thick crosses). The thick lines indicate our lower and upper limits on the star formation density, which are calculated in §4.2

using samples defined in §2.5. The lower limit is very firm, since it includes only those sources with spectroscopic redshifts and identifications with spirals, irregulars and mergers, and does not include the star formation in galaxies fainter than the survey detection limit. The upper limit is also firm, since it includes *all* detected radio sources, even those not associated with star forming galaxies, but is more uncertain than the lower limit since it includes sources without spectroscopic redshifts.

If we were to assume a different cosmology, our results would change somewhat. The values of H_0 , Ω_m , and Ω_Λ affect the calculation of distance from redshift, and luminosity from flux density. The star formation density is proportional to luminosity/volume, so it is inversely proportional to distance and directly proportional to H_0 . If we had assumed $H_0=100 \text{ km s}^{-1}\text{Mpc}^{-1}$ instead of $H_0=50 \text{ km s}^{-1}\text{Mpc}^{-1}$, our data points and model for the star formation density would be twice as large. The values of Ω_m and Ω_Λ also affect the distance measurement. As an extreme example, in a nearly empty but flat universe ($\Omega_m=0.1$, $\Omega_\Lambda=0.9$), the distance to a $z = 1$ object is about 1.5 times larger than the distance to it in our assumed cosmology ($\Omega_m=1$, $\Omega_\Lambda=0$), and thus the star formation density would be about 2/3 of our listed value. Note that all data points in Figures 1 and 10 depend similarly on these cosmological parameters.

At low redshifts, we agree with the findings of many studies that star formation density increases rapidly from the local universe to $z = 1$. We disagree with Cowie, Songaila, & Barger (1999) who find a gradual (rather than steep) increase from $z = 0$ to $z = 1$, and with Mobasher et al. (1999) who find a *decrease* in star formation density $z = 0$ to $z = 1$. Our firm lower limit is significantly higher $z < 1$ than the *extinction corrected* optical results of Lilly et al. (1996) at $z \lesssim 0.7$, indicating that some star formation has been obscured by dust. Our “middle sample” data points fall above all the optical and ultraviolet studies shown, indicating that these studies have probably missed some star formation by underestimating the dust extinction (see Hopkins et al. 2000 for SFR-dependent dust corrections that bring these data more into agreement with our radio results). Our results are similar to the star formation density from the Infrared Space Observatory (ISO) survey of the HDF (Rowan-Robinson et al. 1997).

At redshifts above $z = 1$, we cannot draw strong conclusions. There are few sources with spectroscopic redshifts in this range, so our calculations are based in large part on less secure photometric redshift estimates and random redshift assignments for the very red objects (§2.3). Our assumption that the relationship between radio luminosity and star formation rate does not evolve also becomes less sure as we move to higher redshift (see discussion in §4.1). The Initial Mass Function may also be evolving, although this would affect optical and ultraviolet estimates of star formation history as well. Finally, the faint source corrections (eq. 19, Table 5) become larger at high redshift, and thus depend more strongly on the assumed shape of the luminosity function. In fact, at redshifts above 1.5, the current radio survey limits only probe the extreme end of the luminosity function (SFR per galaxy $> 1000M_\odot$). Deeper surveys are needed to detect radio counterparts to typical high-redshift optical objects, *e.g.* Lyman break galaxies (for instance, the predicted radio fluxes for even the most luminous Lyman break galaxies in the HDF are only a

few μJy at 1.4 GHz, *e.g.* Meurer, Heckman, & Calzetti 1999). Planned improvements to the VLA will allow future surveys to reach this sensitivity.

Still, our calculations at high redshift show that if even a small number of star-forming radio sources exist beyond $z \sim 1.5$, they would indicate a large, optically-hidden fraction of star-formation density. In particular, the population of radio sources with faint, red optical counterparts may be dust-enshrouded (Richards et al. 1999; Barger et al. 2000; Waddington et al. 1999, §2.4), and hence missed even in the deepest optical and ultraviolet studies. Deeper high resolution radio observations, accompanied by close to complete spectroscopic identifications, are needed to determine accurately the amount of “hidden” star formation in the early Universe.

Acknowledgments

D.B.H. and R.B.P. acknowledge the support of NSF grant AST 96-16971 and the Keck Northeast Astronomy Consortium. D.B.H. acknowledges the support of a Cottrell College Science Award from Research Corporation. E.A.R. acknowledges support from Hubble Fellowship Grant HG-0123.01-99A, and from STScI which is operated by AURA under NASA contract NAS 5-26555. R.A.W. acknowledges support from AST-8821016 and AST-9802963 from the National Science Foundation and NASA grants AR-6948.04-96A and GO-7452.01-96A from STScI under NASA contract NAS5-26555. We are grateful to James Lowenthal for providing us with spectroscopic redshifts in advance of publication. We thank Ian Waddington, Ed Fomalont, Ken Kellermann, and Andrew Hopkins for helpful comments and discussions, and our anonymous referee for detailed and helpful comments on the manuscript.

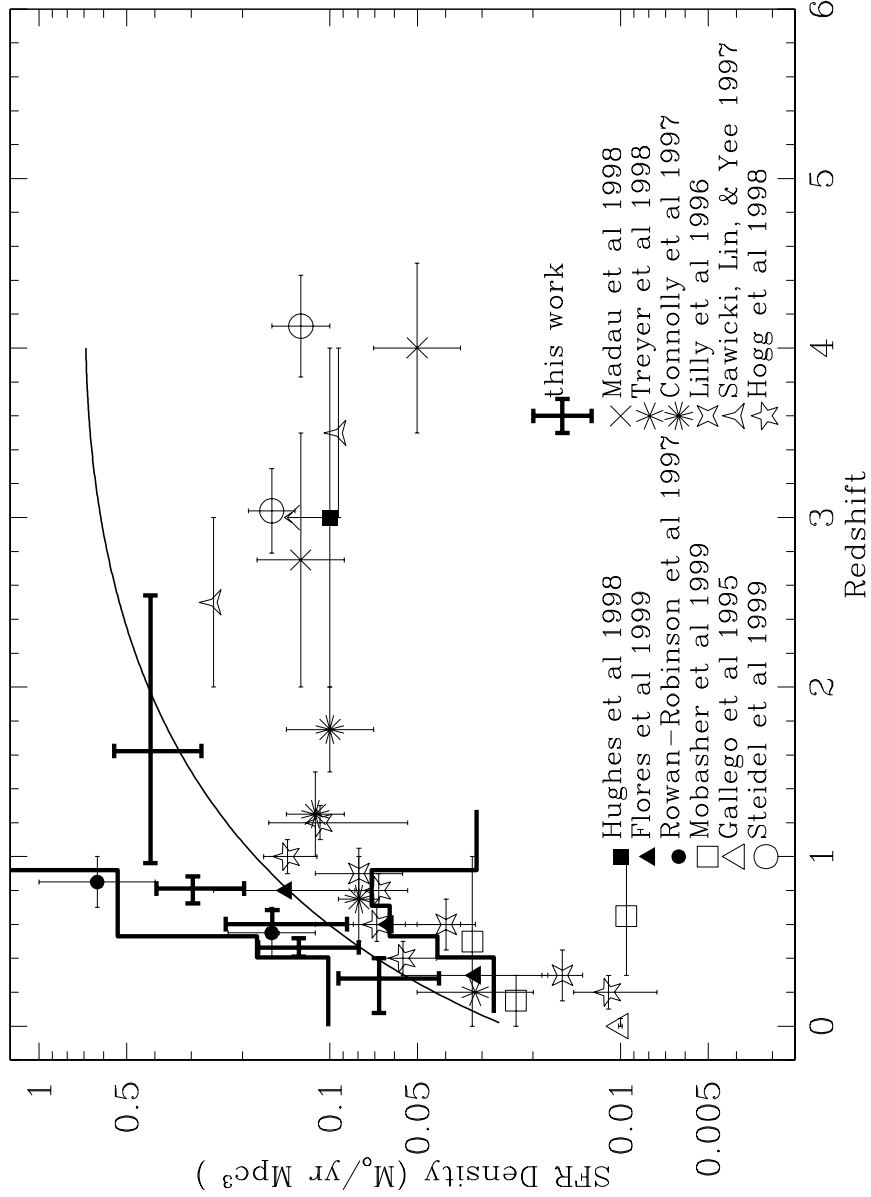


Fig. 10.— Star formation history. Data points are the same as in Figure 1, with our results overlaid. The thick crosses show the star formation density of our middle sample (defined in §2.5), with error bars indicating Poisson errors. The thin curve is our model prediction, found in §4.3 by fitting to the redshift distribution, luminosity function, and extragalactic radio background (not to the heavy crosses shown). The thick lines indicate firm lower and upper limits on the star formation density, calculated in §4.2 using samples defined in §2.5.

REFERENCES

- Barger, A. J., Cowie, L. L., & Richards, E. A. 2000, astro-ph/0001096
- Barger, A. J., Cowie, L. L., Trentham, N., Fulton, E., Hu, E. M., Songaila, A., & Hall, D. 1999, AJ, 117, 102
- Baugh, C. M., Cole, S., Frenk, C. S., & Lacey, C. G. 1998, ApJ, 498, 504
- Benn, C. R., Rowan-Robinson, M., McMahon, R. G., Broadhurst, T. J., & Lawrence, A. 1993, MNRAS, 263, 98
- Brinchmann, J., et al. 1998, ApJ, 499, 112
- Bruzual, A. G., & Charlot, S. 1993, ApJ, 405, 538
- Cohen, J., Hogg, D., Blandford, R., Cowie, L., Hu, E., Songaila, A., Shopbell, P., & Richberg, K. 2000, preprint astro-ph/9912048
- Cohen, J. G., Cowie, L. L., Hogg, D. W., Songaila, A., Blandford, R., Hu, E. M., & Shopbell, P. 1996, ApJ, 471, L5
- Condon, J. J. 1984a, ApJ, 287, 461
- Condon, J. J. 1984b, ApJ, 284, 44
- Condon, J. J. 1989, ApJ, 338, 13
- Condon, J. J. 1992, ARA&A, 30, 575
- Condon, J. J., Anderson, M. L., & Helou, G. 1991, ApJ, 376, 95
- Connolly, A. J., Szalay, A. S., Dickinson, M., SubbaRao, M. U., & Brunner, R. J. 1997, ApJ, 486, L11
- Cowie, L. L., Songaila, A., & Barger, A. J. 1999, AJ, 118, 603
- Cowie, L. L., Songaila, A., Hu, E. M., & Cohen, J. G. 1996, AJ, 112, 839
- Cram, L. 1998, ApJ, 506, L85
- Cram, L., Hopkins, A., Mobasher, B., & Rowan-Robinson, M. 1998, ApJ, 507, 155
- Downes, D., et al. 1999, A&A, 347, 809
- Dwek, E., et al. 1998, ApJ, 508, 106
- Elmegreen, B. G. 1999, ApJ, 515, 323
- Flores, H., et al. 1999, ApJ, 517, 148

- Fomalont, E. B., Kellermann, K. I., Windhorst, R. A., & Kristian, J. A. 1991, *AJ*, 102, 1258
- Gallego, J., Zamorano, J., Aragón-Salamanca, A., & Rego, M. 1995, *ApJ*, 455, L1
- Gould, A., Bahcall, J. N., & Flynn, C. 1996, *ApJ*, 465, 759
- Gruppioni, C., Mignoli, M., & Zamorani, G. 1999, *MNRAS*, 304, 199
- Haarsma, D. B., & Partridge, R. B. 1998, *ApJ*, 503, L5
- Haarsma, D. B., & Partridge, R. B. 1999, in *After the dark ages: when galaxies were young. 9th Astrophysics Conference, College Park Maryland, October 1998*, ed. S. S. Holt & E. P. Smith (Woodbury, New York: AIP), 345
- Hammer, F. 1996, in *Science with the Hubble Space Telescope II*, ed. P. Benvenuti, F. D. Machetto, & E. J. Schreier (Baltimore: Space Telescope Science Institute), 101
- Hammer, F., Crampton, D., Lilly, S. J., LeFevre, O., & Kenet, T. 1995, *MNRAS*, 276, 1085
- Hauser, M. G., et al. 1998, *ApJ*, 508, 25
- Helou, G., Soifer, B. T., & Rowan-Robinson, M. 1985, *ApJ*, 298, L7
- Hogg, D. W., Cohen, J. G., Blandford, R., & Pahre, M. A. 1998, *ApJ*, 504, 622
- Hopkins, A., Afonso, J., Cram, L., & Mobasher, B. 1999, *ApJ*, 519, L59
- Hopkins, A., Connolly, A., Haarsma, D. B., & Cram, L. 2000, submitted
- Hopkins, A. M., Mobasher, B., Cram, L., & Rowan-Robinson, M. 1998, *MNRAS*, 296, 839
- Hughes, D., et al. 1998, *Nature*, 394, 241
- Kellermann, K. I., et al. 2000, in preparation
- Le Fevre, O., Crampton, D., Hammer, F., Lilly, S. J., & Tresse, L. 1994, *ApJ*, 423, L89
- Lilly, S. J., Eales, S. A., Gear, W. K. P., Hammer, F., Le Fèvre, O., Crampton, D., Bond, J. R., & Dunne, L. 1999, *ApJ*, 418, 641
- Lilly, S. J., Le Fèvre, O., Hammer, F., & Crampton, D. 1996, *ApJ*, 460, L1
- Lowenthal, J. D., et al. 1997, *ApJ*, 481, 673
- Madau, P., Ferguson, H. C., Dickinson, M. E., Giavalisco, M., Steidel, C. C., & Fruchter, A. 1996, *MNRAS*, 283, 1388
- Madau, P., Pozzetti, L., & Dickinson, M. 1998, *ApJ*, 498, 106
- Meurer, G. R., Heckman, T. M., & Calzetti, D. 1999, *ApJ*, 521, 64

- Mobasher, B., Cram, L., Georgakakis, A., & Hopkins, A. 1999, MNRAS, 308, 45
- Oort, M. J. A., & Windhorst, R. A. 1985, A&A, 145, 405
- Pascarelle, S. M., Lanzetta, K. M., & Fernández-Soto, A. 1998, ApJ, 508, L1
- Press, W. H., Flannery, B. P., Teukolsky, S. A., & Vetterling, W. T. 1992, Numerical Recipes (2nd ed.) (Cambridge: Cambridge University Press)
- Richards, E. A. 1999, ApJ, 513, L9
- Richards, E. A. 2000, ApJ, 533, 611
- Richards, E. A., Fomalont, E. B., Kellermann, K. I., Windhorst, R. A., Partridge, R. B., Cowie, L. L., & Barger, A. J. 1999, ApJ, 526, L73
- Richards, E. A., Kellermann, K. I., Fomalont, E. B., Windhorst, R. A., & Partridge, R. B. 1998, AJ, 116, 1039
- Rowan-Robinson, M., et al. 1997, MNRAS, 289, 490
- Rowan-Robinson, M., Benn, C. R., Lawrence, A., McMahon, R. G., & Broadhurst, T. J. 1993, MNRAS, 263, 123
- Sawicki, M. J., Lin, H., & H. K. C. Yee. 1997, AJ, 113, 1
- Steidel, C. C., Adelberger, K. L., Gavalisco, M., Dickinson, M., & Pettini, M. 1999, ApJ, 519, 1
- Tresse, L., & Maddox, S. J. 1998, in The Young Universe: Galaxy Formation and Evolution at Intermediate and High Redshift, ed. S. D’Odorico, A. Fontana, & E. Giallongo (ASP Conference Series), 326
- Treyer, M. A., Ellis, R. S., Milliard, B., Donas, J., & Bridges, T. J. 1998, MNRAS, 300, 303
- Waddington, I., Windhorst, R. A., Cohen, S. H., Partridge, R. B., Spinrad, H., & Stern, D. 1999, ApJ, 526, L77
- Windhorst, R. A., et al. 1994a, AJ, 107, 930
- Windhorst, R. A., Fomalont, E. B., Kellermann, K. I., Partridge, R. B., Richards, E., Franklin, B. E., Pascarelle, S. M., & Griffiths, R. E. 1995, Nature, 375, 471
- Windhorst, R. A., Fomalont, E. B., Partridge, R. B., & Lowenthal, J. D. 1993, ApJ, 405, 498
- Windhorst, R. A., Gordon, J. M., Pascarelle, S. M., Schmidtke, P. C., Keel, W. C., Burkey, J. M., & Dunlop, J. S. 1994b, ApJ, 435, 577
- Windhorst, R. A., Mathis, D., & Neuschaefer, L. 1990, in Evolution of the universe of galaxies, ed. R. G. Kron (San Francisco: Astronomy Society of the Pacific), 389

Table 1. Summary of Radio Surveys

Field	Location	Band	Flux limit at field center	Field size (amin ²)	N	N_{sp}	N_{ph}	N_a
Hubble Deep Field (Richards et al. 1998)	12h+62d	8 GHz	$9 \mu\text{Jy}$	66	29	19	4	6
SSA13 field (Windhorst et al. 1995)	13h+42d	8 GHz	$8.8 \mu\text{Jy}$	7	15	8	3	4
V15 field (Fomalont et al. 1991; Hammer et al. 1995)	14h+52d	5 GHz	$16 \mu\text{Jy}$	86	33	18	3	12
Total					77	45	10	22

Note. — The listed flux limit for each field is approximately 5 times the RMS noise at the beam center. The field size is the region in which both radio and optical data are available (see Tables 2, 3, and 4 for details). N is the total number of sources above the flux limit, N_{sp} is the number of those sources with spectroscopic redshifts, N_{ph} is the number with redshifts estimated from I or HK' band magnitudes, and N_a is the number with redshifts randomly assigned (see §2.3 for how assignments were made).

Table 2. HDF

Name	S_8 (μJy)	$S_{1.4}$ (μJy)	α	B_i ($1/\text{asec}^2$)	galtype	ztype	z	HK' (mag)	I (mag)	z_{max}	$\log(L_{e,1.4})$ ($\log[W/Hz]$)	SFR (M_\odot/yr)	Sample
1	2	3	4	5	6	7	8	9	10	11	12	13	14
3632+1105	21.8	(23)	<0.03	0.037	sim	sp ^d	0.518	17.22	19.79	0.785	22.49	37	UML
3634+1212	56.5	211	0.74	0.019	sim	sp ^{cd}	0.458	16.38	19.10	0.966	23.45	340	UML
3634+1240	52.6	198	0.74	0.020	sim	sp ^{ac}	1.219	19.11	22.29	2.34	24.49	3700	UML
3637+1135	17.5	(23)	<0.15	0.049	sim	sp ^a	0.078	17.07	18.61	0.108	20.78	1	UML
3640+1010	29.2	65	0.45	0.029	fr	afr	1.1	21.22	>25	1.78	23.80	750	U
3641+1142	18.6	30	0.27	0.045	sim	sp ^d	0.548	19.26	22.07	0.759	22.70	61	UML
3642+1331	79.9	432	0.94	0.016	el	sp ^e	4.42	21.23	>25	9.12	26.52	...	U
3642+1545	53.6	131	0.50	0.020	un(sim)	sp ^{cd}	0.857	18.07	20.86	1.76	23.85	860	UM
3644+1133	752	1290	0.30	0.015	el	sp ^{ac}	1.050	17.64	21.04	6.38	25.00	...	U
3644+1249	10.2	(21)	(0.4)	0.249	sim	sp ^a	0.557	18.30	20.59	0.589	22.59	47	UML
3646+1404	190	177	-0.04	0.015	sim	sp ^{abc}	0.962	18.19	20.75	3.85	23.95	1100	UML
3646+1447	13.3	77	0.98	0.081	el	ph	0.69	20.21	22.05	0.804	23.50	<390	U
3646+1448	24.7	112	0.84	0.033	fr	afr	1.5	>22	>25	2.16	24.52	4000	U
3649+1313	14.0	51	0.72	0.072	sim	sp ^{ac}	0.475	18.68	21.10	0.575	22.87	90	UML
3651+1030	26.0	99	0.74	0.031	sim	sp ^{abc}	0.410	17.37	19.89	0.638	23.01	120	UML
3651+1221	16.8	60	0.71	0.052	fr	afr	1.7	>21.5	>25	2.16	24.34	2700	U
3652+1444	185	148	-0.12	0.015	el	sp ^{abc}	0.322	16.53	18.70	1.35	22.84	<83	U
3653+1139	15.1	60	0.77	0.062	sim	sp ^{cd}	1.275	19.44	21.90	1.55	24.04	1300	UML
3655+1311	12.3	(23)	<0.35	0.102	el	sp ^d	0.968	18.62	21.62	1.11	23.18	<180	U
3657+1455	15.3	(23)	<0.23	0.061	un(sim)	sp ^d	0.859	18.83	21.44	1.07	23.01	120	UM
3700+0908	66.7	326	0.89	0.018	fr	afr	2.9	20.98	>25	5.75	25.82	...	U
3701+1146	29.5	98	0.67	0.028	fr	sp ^{cd}	0.884	20.14	24.81	1.41	23.80	770	UM
3707+1408	29.0	49	0.29	0.029	fr	ph	2.07	20.29	24.70	3.35	24.28	2300	UM
3708+1056	26.4	49	0.35	0.031	sim	sp ^{cd}	0.423	17.91	19.87	0.684	22.68	57	UML
3708+1246	19.5	(23)	<0.09	0.042	sim	ph	0.887	19.82	21.73	1.24	23.01	120	UM
3711+1331	31.1	108	0.69	0.027	sim	ph	1.53	19.59	22.75	2.42	24.47	3600	UM
3716+1512	85.8	180	0.41	0.016	sim	sp ^c	0.558	17.36	19.80	1.45	23.53	410	UML
3721+1129	630	383	-0.28	0.015	fr	afr	2.5	20.90	>25	>10	25.07	...	U
3725+1128	530	5960	1.35	0.015	fr	afr	2.7	>21.5	>25	9.12	27.25	...	U

^aCohen et al. (1996)

^bLowenthal et al. (1997)

^cBarger et al. (2000)

^dCohen et al. (2000)

^eWaddington et al. (1999)

Note. — These sources are cataloged by Richards et al. (1998) who gives the detailed source positions. Sources are included here only if they are within $4.6'$ of the radio field center and above the 8 GHz radio flux limit of Richards et al. (1998) (additional sources were detected in Richards 2000 but are not included because of their complicated primary beam corrections and lack of spectroscopic redshifts). The flux measurements, S_8 and $S_{1.4}$, are from Richards (2000). Several sources were identified as faint/red by Richards et al. (1999). The I and HK' magnitudes are from Barger et al. (1999). The remaining quantities in the table are calculated or assigned in this work.

Table 3. SSA13

Name	S_8 (μJy)	$S_{1.4}$ (μJy)	α	B_i ($1/\text{asec}^2$)	galtype	ztype	z	HK' (mag)	I (mag)	z_{max}	$\log(L_{e,1.4})$ ($\log[W/Hz]$)	SFR (M_\odot/yr)	Sample
1	2	3	4	5	6	7	8	9	10	11	12	13	14
(1) 1214+3822	8.9	(18)	(0.4)	0.245	fr	afr	1.5	21.95	> 25	1.51	23.56	440	U
(3) 1215+3703	14.1	(29)	(0.4)	0.141	un(sim)	sp	0.322	18.70	20.81	0.398	22.19	19	UM
(5) 1216+3921	33.7	(69)	(0.4)	0.141	fr	afr	2.3	> 25	> 25	3.94	24.60	4800	U
(6) 1217+3913	24.1	(49)	(0.4)	0.141	un(sim)	sp	0.494	17.57	19.99	0.767	22.84	84	UM
(7) 1218+3931	15.1	(31)	(0.4)	0.141	fr	ph	2.54	21.22	> 25	3.16	24.36	2800	UM
(9) 1218+3844	26.6	(45)	(0.4)	0.141	un(el)	sp	0.698	17.57	20.62	1.12	23.23	<210	U
(10) 1220+3833	18.3	(37)	(0.4)	0.141	un(sim)	a	0.559	21.78	24.08	0.767	22.85	85	U
(11) 1220+3703	14.3	(29)	(0.4)	0.141	fr	ph	2.02	20.77	> 25	2.45	24.08	1500	UM
(12) 1220+3923	14.3	(29)	(0.4)	0.141	fr	afr	1.9	23.36	> 25	2.32	24.02	1300	U
(13) 1221+3923	10.1	(21)	(0.4)	0.225	sim	sp	0.302	17.08	19.42	0.323	21.99	12	UML
(15) 1221+3723	18.3	(37)	(0.4)	0.141	sim	sp	0.180	17.04	18.99	0.254	21.76	7	UML
(16) 1222+3827	17.4	(36)	(0.4)	0.141	un(sim)	ph	0.685	19.38	22.03	0.923	23.03	130	UM
(18) 1223+3909	21.1	(43)	(0.4)	0.141	un(el)	sp	0.765	17.19	19.92	1.11	23.23	<200	U
(19) 1224+3712	29.2	(60)	(0.4)	0.141	un(sim)	sp	0.401	16.68	19.14	0.684	22.72	63	UM
(24) 1228+3800	23.8	(49)	(0.4)	0.141	sim	sp	0.316	17.04	19.60	0.495	22.40	30	UML

Note. — These sources are cataloged by Windhorst et al. (1995) (catalog number in parentheses) who gives the detailed source positions; the source name is derived from its radio position. Sources are included here if they are above the radio flux limit of Kellermann et al. (2000), fully within the optical field of Windhorst et al. (1995), and not identified with quasars or stars. The I and HK' magnitudes are from Cowie et al. (1996). The S_8 flux densities are from Kellermann et al. (2000). Sources 1, 5, 7, 11, and 12 are classified as faint/red by Richards et al. (1999). The spectroscopic redshifts for sources 3, 13, 15, and 19 are from Windhorst et al. (1994a), and for sources 6, 9, 18, and 24 are from J. Lowenthal (private communication). The remaining quantities in the table are calculated or assigned in this work.

Table 4. V15

Name	S_5	$S_{1.4}$	α	B_i	galtype	ztype	z	HK'	I	z_{max}	$\log(L_{e,1.4})$	SFR	Sample
1	(μJy) 2	(μJy) 3	4	($1/\text{asec}^2$) 5	6	7	8	(mag) 9	(mag) 10	11	($\log[W/Hz]$) 12	(M_\odot/yr) 13	14
15V05	41	96	0.68	0.019	sim	sp	0.989	...	22.04	1.42	23.92	1000	UML
15V10	1912	2560	0.23	0.012	el	a	0.180	20.86	22.27	1.53	23.58	<460	U
15V11	70	171	0.71	0.014	sim	sp	0.375	...	19.86	0.700	23.16	170	UML
15V15	24	(40)	(0.4)	0.034	el	a	0.302	...	22.30	0.363	22.27	<22	U
15V18	44	(73)	(0.4)	0.018	fr	ph	2.0	21.1	>25	2.99	24.47	3600	UM
15V19	24	(43)	(0.4)	0.034	sim	sp	0.754	...	21.17	0.902	23.17	180	UML
15V21	298	807	0.80	0.012	sim	sp	0.724	...	21.29	2.19	24.53	4100	UML
15V23	54	(80)	<0.31	0.016	el*	sp	1.149	...	21.08	1.91	23.89	930	U
15V24	79	141	0.46	0.014	sim	sp	0.660	19.22	20.64	1.29	23.60	480	UML
15V26a	23	(38)	(0.4)	0.037	el*	sp	0.372	...	21.87	0.442	22.45	<34	U
15V26b	24	(40)	(0.4)	0.034	el*	sp	0.155	...	19.27	0.188	21.64	<5	U
15V28	74	(80)	<0.6	0.014	el	sp	0.988	19.99	21.74	1.95	23.66	<550	U
15V33	20	(33)	(0.4)	0.054	el	a	0.410	...	23.2	0.457	22.49	<37	U
15V34	1311	1160	-0.10	0.012	el	sp	0.838	...	22.01	6.46	24.62	...	U
15V37	51	(80)	<0.36	0.016	el	ph	2.52	20.53	23.65	4.03	24.74	...	U
15V39	35	(58)	(0.4)	0.021	el	sp	0.992	19.89	21.85	1.38	23.62	<500	U
15V40	33	106	0.93	0.022	el	sp	0.976	19.67	21.94	1.29	24.02	<1300	U
15V45	33	150	1.21	0.022	el	a	0.475	...	24.3	0.631	23.42	<320	U
15V47	53	131	0.72	0.016	sim	sp	0.809	22.23	23.00	1.30	23.85	850	UML
15V48	20	(33)	(0.4)	0.054	sim	sp	0.743	...	21.11	0.822	23.08	150	UML
15V49	31	96	0.90	0.023	un(sim)	ph	0.537	19.22	19.96	0.700	23.31	180	UM
15V50	705	1722	0.71	0.012	un(el)	a	0.654	...	22.76	2.79	24.74	...	U
15V51	41	(68)	(0.4)	0.019	un(sim)	a	0.724	...	23.14	1.08	23.36	280	U
15V53	30	85	0.83	0.024	sim	a	0.754	...	23.04	0.966	23.61	490	U
15V57	37	(61)	(0.4)	0.020	el*	sp	0.010	17.83	17.70	0.0153	19.40	<1	U
15V59	19	(31)	(0.4)	0.066	un(sim)	a	0.960	...	24.5	1.04	23.32	250	U
15V60	39	(64)	(0.4)	0.019	sim	sp	0.812	...	21.94	1.19	23.46	350	UML
15V62	24	(40)	(0.4)	0.034	fr	afr	2.1	>21.3	>25	2.48	24.26	2200	U
15V67	46	(76)	(0.4)	0.017	fr	afr	2.5	...	>25	3.80	24.73	...	U
15V70	576	2414	1.14	0.012	fr	afr	1.3	...	>25	4.27	25.80	...	U
15V72	46	(76)	(0.4)	0.017	el	a	1.219	20.9	23.8	1.88	23.96	1100	U
15V73	37	(61)	(0.4)	0.020	el	sp	0.746	...	20.95	1.07	23.35	<270	U
15V81	28	(46)	(0.4)	0.026	el*	sp	1.158	...	22.16	1.46	23.69	<590	U

Note. — These sources are cataloged by Fomalont et al. (1991), who gives detailed source positions and the 5 GHz and 1.4 GHz flux densities. Sources are not included here if they are quasars, stars, below the radio flux limit, or outside the optical field of Hammer et al. (1995). Sources 30, 36, 41, and 69 were found later to be pairs of radio sources, with both members of the pair below the radio flux limit, and so are not included. The galaxy types, spectroscopic redshifts, and I and K magnitudes are from Hammer et al. (1995). An asterisk (*) indicates that Hammer et al. (1995) classified the galaxy type based on its emission lines, which they find to be more characteristic of AGN than starbursts. The spectroscopic redshifts for 15V5 and 15V47, and the galaxy type for 15V47, are from Brinchmann et al. (1998). Lilly et al. (1999) finds a photometric redshift of 2 for 15V18. Flores et al. (1999) identifies source 23 as a Seyfert 2 galaxy. The remaining quantities in the table are calculated or assigned in this work.

Table 5. Faint Source Correction Factors

Redshift	Correction factor $C(z)$	
	8 GHz, $S_{lim} = 9 \mu\text{Jy}$	5 GHz, $S_{lim} = 16 \mu\text{Jy}$
0.28	1.3	1.5
0.46	1.6	2.0
0.60	1.9	2.3
0.81	2.2	3.0
1.6	3.8	5.8

Table 6. Star Formation History

Redshift		SFR Density ($M_{\odot}\text{yr}^{-1}\text{Mpc}^{-3}$)		
Average ^a	Range ^b	Value from Middle Sample	Poisson error range	Lower and Upper Limits
0.28	0.010-0.401	0.068	0.042-0.093	0.027-0.101
0.46	0.410-0.518	0.128	0.080-0.176	0.043-0.178
0.60	0.548-0.698	0.158	0.087-0.228	0.062-0.537
0.81	0.724-0.884	0.296	0.197-0.395	0.072-0.536
1.6	0.960-4.42	0.414	0.276-0.552	0.031-15.5

^aaverage redshift in bin from middle sample

^brange of redshifts in bin from upper sample